Natural oscillations of underactuated cable-driven parallel robots

(Article begins on next page)

17 July 2024

Natural Oscillations of Underactuated Cable-Driven Parallel Robots

EDOARDO IDÀ[1], (Member, IEEE), SÉBASTIEN BRIOT[2], and MARCO CARRICATO[1], (Senior Member, IEEE)

[1]Dept. of Industrial Engineering, University of Bologna, 40137 Bologna, Italy (e-mails: edoardo.ida2@unibo.it, marco.carricato@unibo.it)
[2]Centre National de la Recherche Scientifique (CNRS) at the Laboratoire des Sciences du Numérique de Nantes (LS2N), UMR CNRS 6004, 44300 Nantes, France (e-mail: Sebastien.Briot@ls2n.fr)

Corresponding author: Edoardo Idà (e-mail: edoardo.ida2@unibo.it).

ABSTRACT Underactuated Cable-Driven Parallel Robots (*CDPR*) employ a number of cables smaller than the degrees of freedom (*DoFs*) of the end-effector (*EE*) that they control. As a consequence, the *EE* is underconstrained and preserves some freedoms even when all actuators are locked, which may lead to undesirable oscillations. This paper proposes a methodology for the computation of the *EE* natural oscillation frequencies, whose knowledge has proven to be convenient for control purposes. This procedure, based on the linearization of the system internal dynamics about equilibrium configurations, can be applied to a generic robot suspended by any number of cables comprised between 2 and 5. The kinematics, dynamics, stability and stiffness of the robot free motion are investigated in detail. The validity of the proposed method is demonstrated by experiments on 6-*DoF* prototypes actuated by 2, 3, and 4 cables. Additionally, in order to highlight the interest in a robotic context, this modelling strategy is applied to the trajectory planning of a 6-*DoF* 4-cable *CDPR* by means of a frequency-based method (multi-mode input shaping), and the latter is experimentally compared with traditional non-frequency-based motion planners.

INDEX TERMS Cable-driven parallel robots, frequency analysis, input shaping, underactuated robots, underconstrained robots.

NOMENCLATURE

Geometric symbols
$\mathbf{p}$	*EE* position
$\boldsymbol{\epsilon}$	*EE* orientation
$\boldsymbol{\zeta}$	*EE* pose
$\boldsymbol{\zeta}_f$	*EE* free pose coordinates
$\boldsymbol{\zeta}_d$	*EE* dependent pose coordinates
$\mathbf{d}_i$	cable entry point in the pulley
$\mathbf{b}_i$	cable exit point from the pulley
$\mathbf{a}_i$	cable attachment point on the *EE*
$\mathbf{k}_i$	swivel-axis unit vector
$\mathbf{w}_i$	unit vector normal to the pulley plane
$\mathbf{u}_i$	$\mathbf{w}_i \times \mathbf{k}_i$
$\mathbf{t}_i$	unit vector along the cable
$\mathbf{n}_i$	$\mathbf{t}_i \times \mathbf{w}_i$
$\boldsymbol{\rho}_i$	$\mathbf{a}_i - \mathbf{b}_i$ (cable vector)
σ_i	swivel angle
ψ_i	tangency angle
l_i	cable length

Kinematic symbols
$\boldsymbol{\omega}$	*EE* angular velocity
$\mathbf{v}$	*EE* twist
$\boldsymbol{\xi}_i$	0-pitch screw directed as $\mathbf{t}_i$ passing through A_i
$\boldsymbol{\Xi}$	kinematic Jacobian
$\boldsymbol{\Xi}^{\perp}$	nullspace of the kinematic Jacobian
$\mathbf{J}$	analytical Jacobian
$\mathbf{J}^{\perp}$	nullspace of the analytical Jacobian
$\mathbf{P}$	permutation matrix

Dynamic symbols
$\mathbf{s}$	position of the center of mass G
$\mathbf{I}_G$	*EE* inertia tensor about G
$\mathbf{M}$	*EE* Mass matrix
$\mathbf{C}$	*EE* Coriolis matrix
$\boldsymbol{\tau}$	cable-tension array
$\boldsymbol{\phi}$	resultant of the external forces
$\mathbf{q}$	application point Q of $\boldsymbol{\phi}$
$\boldsymbol{\mu}$	resultant moment of the external forces about Q

K   *UACDPR Geometric Stiffness*
K$^\perp$ *UACDPR Free-Motion Stiffness*
f_j *UACDPR natural oscillation frequency*

I. INTRODUCTION

CABLE-driven parallel robots (*CDPRs*) control the end-effector (*EE*) pose by means of extendable cables. A *CDPR* is underactuated if the number n of actuated cables is smaller than the number of the *EE* degrees of freedom (*DoFs*). As a consequence, only a sub-set of the *EE* coordinates can be directly controlled, with the remaining ones being determined by the system mechanical equilibrium. An underactuated *CDPR* (*UACDPR* in short) is always underconstrained, thus its *EE* preserves some *DoFs* once actuators are locked. Accordingly, in case the *EE* is not in a static equilibrium configuration when actuators cease to move, the *UACDPR* exhibits (possibly dangerous) oscillatory motions. This oscillatory behaviour is naturally expected to occur at the end-point of a trajectory, if suitable motion-planning and control techniques are not employed [1], or it may result from an emergency stop or an actuator failure.

Despite these drawbacks, the use of *CDPRs* with a limited number of cables may be favorable in several applications, in which a limitation of mobility is acceptable in order to enhance workspace accessibility or decrease mechanical complexity and robot cost [2]–[5]. Thus, the study of *UACDPRs* is attracting the interest of more and more researchers, who have dealt with their geometrico-static problems [6], [7], equilibrium stability analysis [8], [9], trajectory planning [1], [10]–[16], system parameter identification [17], and control [18]–[20].

The knowledge of natural oscillation frequencies of *UACDPRs* can be used in order to derive frequency-based trajectory planners based on periodic excitation [11] or input-shaping [12], [14]–[16]: these planners *limit* oscillations, and are *real-time capable*, as opposed to rest-to-rest trajectory planners [1], which can *completely* stop a *UACDPR EE* after a point-to-point motion, but needs to be computed *off-line* (and are not frequency-based). Additionally, natural oscillation frequencies may also be exploited for optimal robot design [21].

In order to compute *UACDPRs* natural oscillation frequencies, the *EE internal dynamics* [1] needs to be derived, and expressed in terms of a minimal set of *EE* residual *DoFs*. Natural frequencies are determined by linearizing, about an equilibrium configuration, the *EE* internal dynamics with respect to (w.r.t.) the *EE* residual *DoFs*, and by solving the resulting eigenproblem. The authors of [11], [12] derived the single configuration-dependent natural oscillation frequency of a planar 3-*DoF* 2-cable robot, by intuitively selecting the platform orientation as the *EE* residual *DoF*, whereas in [15] the same technique was employed for a spatial 6-*DoF* 3-cable system, where *ZYX* Tait-Bryan angles were chosen as residual *DoFs*. Due to the specific *UACDPR* architectures reported in [11],

[12], [15], the translational and rotational mechanical equilibria of the *EE* could be decoupled, which resulted in a mathematically simpler internal dynamics formulation and linearization. This was not the case, instead, for the 6-*DoF* 4-cable manipulator considered in [14], where the authors determined the system natural frequencies with a method similar to the one developed in [12], by approximating the 6-*DoF* robot with two 3-*DoF* planar sub-systems and selecting the orientations of these sub-systems' platforms as residual *DoFs*. In fact, because of the intrinsic coupling of rotational and translational equilibria of 6-*DoF UACDPRs* with more than 3 cables, it is not straightforward to select the corresponding residual *DoFs* (1 *DoF* for 5-cable robots and 2 *DoFs* for 4-cable robots), and to derive and linearize the manipulator internal-dynamic equations: singularities may arise in the computation, which results in the failure of natural frequency determination.

The contributions presented in this paper are the following.
1) A novel unified technique is proposed for the computation of the natural oscillation frequencies of *UACDPRs* with a generic number n of cables ($1 < n < 6$), a generic geometry, and subject to a generic external wrench. Previous works only analyzed specific architectures, such as 2-cable 3-*DoF UACDPRs* [11], [12] and 3-cable 6-*DoF UACDPRs* [15], [16], or an approximation of a 4-cable 6-*DoF UACDPR* with two 2-cable 3-*DoF UACDPRs* [14]. Our approach allows an easy selection of the *EE* residual *DoFs* and the opportunity of easily switching between a selection and another, so that representation singularities may always be avoided in the formulation of the internal dynamics; the subsequent natural frequency computation is performed with a well-known tool, namely linearizing the internal dynamics about an equilibrium configuration. Additionally, the proposed modelling method has the merit of determining out-of-the-plane oscillation frequencies of planar systems with 2 cables, which were not previously considered [11], [12]: the determination of these frequencies proved to be useful in [18], where the authors determined them experimentally, and used them in the design of a stabilizing controller for the robot *EE*.
2) The natural oscillation frequencies of generic medium-scale *UACDPRs* with 2, 3 and 4 cables are experimentally determined and compared with the ones computed by means of the new technique, thus showing that the latter is adequate for real-world applications.
3) The stiffness and equilibrium stability of *UACDPR* are refined w.r.t. the state of the art [8], [9] by taking into account swivel pulleys in the kinematic model and a generic wrench (not necessarily a pure force) acting on the *EE*.
4) The relevance of our modelling technique is demonstrated in the context of frequency-based motion planners, by planning the point-to-point trajectory of a 4-cable 6-*DoF UACDPR* by means of a Multi-Mode Input
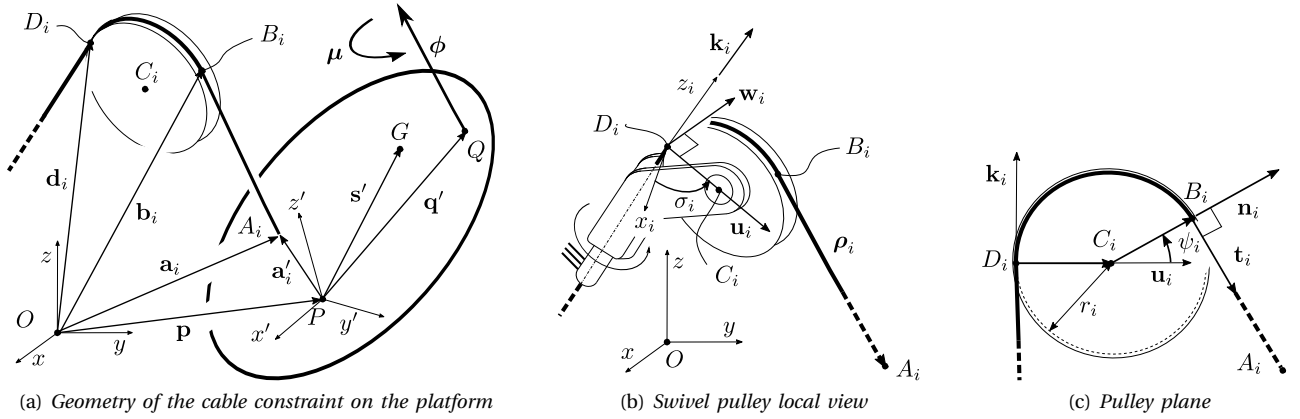
(a) *Geometry of the cable constraint on the platform* (b) *Swivel pulley local view* (c) *Pulley plane*

Figure 1: *CDPR geometric model*

Shaper [22]. The results are experimentally compared with those that can be achieved by non-frequency-based motion planners.

The structure of the paper is as follows. Section II reports the kinematic model. Section III investigates the behaviour of an *UACDPR* when it is in *free motion*, that is, when cable lengths are constant. The computation of natural oscillation frequencies is then carried out in Section IV, while Section V experimentally verifies that the frequencies computed by the proposed approach closely match the ones of physical 2-, 3- and 4-cable *UACDPR* prototypes. Section VI shows an application example: the experimental comparison between an Input-Shaped trajectory of a 4-cable *UACDPR* and other motion planners. Conclusions are drawn in Section VII.

II. KINEMATIC MODEL

The kinematic model of an *UACDPR* is derived by considering the geometric constraints imposed by n (taut) cables, with $1 < n < 6$, on the robot 6-*DoF EE*, as in [1]. The pose $\zeta = [\mathbf{p}^T \boldsymbol{\epsilon}^T]^T$ of the *EE* is described in the inertial frame $Oxyz$ by the position vector $\mathbf{p}$ of P, the *EE* reference point, and a minimal set of angles $\boldsymbol{\epsilon}$ (Fig. 1a).

Cables are assumed to be massless (which is reasonable for small- to medium-scale *CDPRs*), infinitely rigid and always subject to non-zero tensile loads. Additionally, each cable is guided into the workspace by a swivel pulley, which can rotate about its swivel axis. Such a pulley has radius r_i and center C_i, and is mounted on an hinged support, whose swivel axis is tangent to the pulley in point D_i (Figs. 1b,1c). The cable enters the pulley groove in D_i, exits from it at point B_i, and it is attached to the platform at point A_i. $\mathbf{d}_i$ and $\mathbf{a}_i$ are the position vectors of D_i and A_i, whereas $\mathbf{a}'_i$ is a vector pointing from P to A_i. All position vectors, except $\mathbf{d}_i$, are functions of the *EE* pose ζ in $Oxyz$.

The coordinates of position vector $\mathbf{b}_i$ of point B_i, in the inertial frame, depend on ζ and also on the pulley model. $\mathbf{k}_i$, $\mathbf{w}_i$, $\mathbf{u}_i$, $\mathbf{n}_i$, and $\mathbf{t}_i$ are additional unit vectors

associated with the pulley geometry. As shown in Figs. 1b,1c: $\mathbf{k}_i$ is directed along the swivel axis, $\mathbf{u}_i$ points from D_i to C_i, $\mathbf{w}_i = \mathbf{k}_i \times \mathbf{u}_i$ is normal to the plane defined by the swivel axis and the i-th cable, $\mathbf{n}_i$ points from C_i to B_i, $\mathbf{t}_i = \mathbf{w}_i \times \mathbf{n}_i$ is directed as the i-th cable; σ_i and ψ_i are swivel and tangency angles. All these variables depend on the *EE* pose ζ and, in case ζ is known, they can be computed in closed form, as shown in [1]. Accordingly:

$$\mathbf{b}_i = \mathbf{d}_i + r_i (\mathbf{u}_i + \mathbf{n}_i) \tag{1}$$

The constraint imposed by each cable onto the *EE* is:

$$\boldsymbol{\rho}_i^T \boldsymbol{\rho}_i - [\, l_i - r_i (\pi - \psi_i)\,]\,|^2 = 0 \tag{2}$$

where $\boldsymbol{\rho}_i \triangleq \mathbf{a}_i - \mathbf{b}_i$, and l_i is the total cable length, comprising the rectilinear part $\|\boldsymbol{\rho}_i\|$ and the arc $\widehat{B_i D_i}$ wrapped onto the pulley.

A. DIFFERENTIAL KINEMATICS

If $\boldsymbol{\omega}$ is the angular velocity of the *EE*, the *EE* twist is $\mathbf{v} = [\dot{\mathbf{p}}^T \boldsymbol{\omega}^T]^T$ and its linear relationship with $\dot{\zeta}$ is given by:

$$\mathbf{v} = \mathbf{D}(\boldsymbol{\epsilon})\dot{\zeta}, \qquad \mathbf{D}(\boldsymbol{\epsilon}) \triangleq \begin{bmatrix} \mathbf{I}_{3\times3} & \mathbf{0}_{3\times3} \\ \mathbf{0}_{3\times3} & \mathbf{H}(\boldsymbol{\epsilon}) \end{bmatrix} \tag{3}$$

where $\mathbf{I}_{3\times3} \in \mathbb{R}^{3\times3}$ and $\mathbf{0}_{3\times3} \in \mathbb{R}^{3\times3}$ are identity and null matrices, and $\mathbf{H}(\boldsymbol{\epsilon})$ depends on the parametrization used to describe the orientation [1].

The rate of change of l_i, $\dot{l}_i$, can be computed as the projection of the velocity of point A_i along the i-th cable direction $\mathbf{t}_i$ [1], [23], [24], that is:

$$\dot{\mathbf{a}}'_i = \dot{\mathbf{p}} + \boldsymbol{\omega} \times \mathbf{a}'_i \tag{4}$$

$$\dot{l}_i = \mathbf{t}_i \cdot \dot{\mathbf{a}}'_i = \boldsymbol{\xi}_i \cdot \mathbf{v}, \qquad \boldsymbol{\xi}_i \triangleq \begin{bmatrix} \mathbf{t}_i \\ \mathbf{a}'_i \times \mathbf{t}_i \end{bmatrix} \tag{5}$$

where $\boldsymbol{\xi}_i$ is a zero-pitch screw directed as $\mathbf{t}_i$ and passing through A_i, and the symbols · and × denote the scalar

and vector products, respectively. The relationship between the *EE* twist $\mathbf{v}$ and the derivatives of the system actuated variables, $\mathbf{l} = [l_1 \ldots, l_n]^T$, is thus given by:

$$\mathbf{\Xi v} = \dot{\mathbf{l}}, \qquad \mathbf{\Xi} \triangleq [\boldsymbol{\xi}_1 \cdots \boldsymbol{\xi}_n]^T \tag{6}$$

where matrix $\mathbf{\Xi} \in \mathbb{R}^{n \times 6}$ is the kinematic Jacobian of the manipulator. In general, rank$(\mathbf{\Xi}) = n$, but, if a direct-kinematics singularity is encountered [25], rank$(\mathbf{\Xi}) < n$.

By substituting (3) in (6), the relationship between $\dot{\mathbf{l}}$ and the derivative of the *EE* pose is obtained as:

$$\mathbf{\Xi D}\dot{\boldsymbol{\zeta}} = \mathbf{J}\dot{\boldsymbol{\zeta}} = \dot{\mathbf{l}}, \qquad \mathbf{J} \triangleq \mathbf{\Xi D} \tag{7}$$

Matrix $\mathbf{J} \in \mathbb{R}^{n \times 6}$ is the analytic Jacobian of the manipulator, thus it is a proper gradient, which may also be obtained by differentiating (2) w.r.t. $\boldsymbol{\zeta}$ for $i = 1, \cdots, n$ [26].

III. FREE MOTION

The aim of this section is to highlight some kinematic and dynamic properties of the *UACDPR* when actuators are locked, namely $\mathbf{l} = \mathbf{l}_0$, $\dot{\mathbf{l}} = \ddot{\mathbf{l}} = \mathbf{0}_{n \times 1}$, and thus the *EE* is in *free motion*.

A. FREE-MOTION KINEMATICS

The free-motion first-order kinematics can be described by setting $\dot{\mathbf{l}} = \mathbf{0}_{n \times 1}$ in (6):

$$\mathbf{\Xi v} = \mathbf{0}_{n \times 1} \tag{8}$$

namely (cf. (3) and (7)):

$$\mathbf{J}\dot{\boldsymbol{\zeta}} = \mathbf{0}_{n \times 1} \tag{9}$$

Once the lengths of the n cables are set and all cables are taut, that is, all kinematic constraints are active, and $\mathbf{\Xi}$ has full column rank, the *EE* can still move on a variety of dimension $\lambda = 6 - n$ in SE(3), thus preserving λ *DoFs*. Consequently, λ components of $\boldsymbol{\zeta}$ are *free* to vary, and are called *free pose components* $\boldsymbol{\zeta}_f$. The remaining n components of $\boldsymbol{\zeta}$ are called *dependent pose components* $\boldsymbol{\zeta}_d$, since they depend on the value of cable lengths $\mathbf{l}_0$ and free pose components $\boldsymbol{\zeta}_f$. When actuators are locked, the *free twist* $\mathbf{v}$ of the *EE* can be expressed as a function of the *EE* λ residual *DoFs*. This can be done by computing the right nullspace $\mathbf{\Xi}^\perp$ of matrix $\mathbf{\Xi}$. By definition, the right nullspace of the full-rank ($n \times 6$) matrix $\mathbf{\Xi}$ is spanned by the (independent) columns of a ($6 \times \lambda$) matrix $\mathbf{\Xi}^\perp$ such that $\mathbf{\Xi \Xi}^\perp = \mathbf{0}_{n \times \lambda}$, so that its columns define a basis for the free twist $\mathbf{v}$:

$$\mathbf{v} = \mathbf{\Xi}^\perp \mathbf{c} \qquad \text{for some } \mathbf{c} \in \mathbb{R}^\lambda \tag{10}$$

If $\mathbf{J}^\perp$ is the right nullspace of matrix $\mathbf{J}$, then:

$$\mathbf{v} = \mathbf{D}\dot{\boldsymbol{\zeta}} = \mathbf{DJ}^\perp \mathbf{c}' \qquad \text{for some } \mathbf{c}' \in \mathbb{R}^\lambda \tag{11}$$

Comparing (10) and (11) and choosing $\mathbf{c} = \mathbf{c}'$ yields:

$$\mathbf{\Xi}^\perp = \mathbf{DJ}^\perp \tag{12}$$

Equation (12) has great significance in the computation of natural oscillation frequencies of *UACDPR*, as Section IV will highlight.

Since most orientation parametrizations of SO(3) allow rank$(\mathbf{D}) \geq 5$ (even in case of representation singularities), and $5 \geq n$ for any *UACDPR*, one can always assume rank$(\mathbf{D}) \geq n$. This allows us to find an expression of $\mathbf{J}^\perp$, and thus of $\mathbf{\Xi}^\perp$, so that the parameter array $\mathbf{c}$ can be chosen as a subset of $\dot{\boldsymbol{\zeta}}$. Since $\mathbf{\Xi}$ has full column rank and rank$(\mathbf{D}) \geq n$, a permutation matrix[1] $\mathbf{P} \in \mathbb{R}^{6 \times 6}$ can be determined so that:

$$\dot{\boldsymbol{\zeta}}_P \triangleq \mathbf{P}\dot{\boldsymbol{\zeta}} = \begin{bmatrix} \dot{\boldsymbol{\zeta}}_d \\ \dot{\boldsymbol{\zeta}}_f \end{bmatrix}, \qquad \dot{\boldsymbol{\zeta}}_d \in \mathbb{R}^n, \ \dot{\boldsymbol{\zeta}}_f \in \mathbb{R}^\lambda \tag{13}$$

$$\mathbf{J}_P \triangleq \mathbf{JP}^T = \mathbf{\Xi DP}^T = \mathbf{\Xi} \begin{bmatrix} \mathbf{D}_d & \mathbf{D}_f \end{bmatrix} = \begin{bmatrix} \mathbf{J}_d & \mathbf{J}_f \end{bmatrix} \tag{14}$$

$$\mathbf{D}_d \in \mathbb{R}^{6 \times n}, \qquad \mathbf{J}_d \triangleq \mathbf{\Xi D}_d \in \mathbb{R}^{n \times n} \tag{15}$$

$$\mathbf{D}_f \in \mathbb{R}^{6 \times \lambda}, \qquad \mathbf{J}_f \triangleq \mathbf{\Xi D}_f \in \mathbb{R}^{n \times \lambda} \tag{16}$$

$$\mathbf{J}_P^\perp \triangleq \mathbf{PJ}^\perp, \qquad \mathbf{J}_P^\perp, \mathbf{J}^\perp \in \mathbb{R}^{6 \times \lambda} \tag{17}$$

where:

$$\mathbf{JJ}^\perp = \mathbf{JP}^T \mathbf{PJ}^\perp = \mathbf{J}_P \mathbf{J}_P^\perp = \mathbf{0}_{n \times \lambda} \tag{18}$$

The permutation matrix $\mathbf{P}$ must always be chosen so that rank$(\mathbf{D}_d) = n$ and, since rank$(\mathbf{\Xi}) = n$, this also means rank$(\mathbf{J}_d) = n$. This allows us to express $\dot{\boldsymbol{\zeta}}$, and thus $\mathbf{v}$, as a function of $\dot{\boldsymbol{\zeta}}_f$ in free motion. Indeed, since:

$$\mathbf{J}\dot{\boldsymbol{\zeta}} = \mathbf{J}_P \dot{\boldsymbol{\zeta}}_P = \mathbf{J}_d \dot{\boldsymbol{\zeta}}_d + \mathbf{J}_f \dot{\boldsymbol{\zeta}}_f = \mathbf{0}_{n \times 1} \tag{19}$$

then:

$$\dot{\boldsymbol{\zeta}}_d = -\mathbf{J}_d^{-1} \mathbf{J}_f \dot{\boldsymbol{\zeta}}_f \tag{20}$$

$$\dot{\boldsymbol{\zeta}}_P = \mathbf{J}_P^\perp \dot{\boldsymbol{\zeta}}_f, \qquad \mathbf{J}_P^\perp = \begin{bmatrix} -\mathbf{J}_d^{-1} \mathbf{J}_f \\ \mathbf{I}_{\lambda \times \lambda} \end{bmatrix} \tag{21}$$

$$\dot{\boldsymbol{\zeta}} = \mathbf{P}^T \dot{\boldsymbol{\zeta}}_P = \mathbf{P}^T \mathbf{J}_P^\perp \dot{\boldsymbol{\zeta}}_f = \mathbf{J}^\perp \dot{\boldsymbol{\zeta}}_f, \qquad \mathbf{J}^\perp = \mathbf{P}^T \mathbf{J}_P^\perp \tag{22}$$

$$\mathbf{v} = \mathbf{D}\dot{\boldsymbol{\zeta}} = \mathbf{DJ}^\perp \dot{\boldsymbol{\zeta}}_f = \mathbf{\Xi}^\perp \dot{\boldsymbol{\zeta}}_f, \qquad \mathbf{\Xi}^\perp = \mathbf{DP}^T \mathbf{J}_P^\perp = \mathbf{DJ}^\perp \tag{23}$$

Matrix $\mathbf{J}_P^\perp$ in (21) always satisfies (18). Basically, matrix $\mathbf{P}$ allows us to group n dependent pose-derivative components in $\dot{\boldsymbol{\zeta}}_d$ and λ free pose-derivative components in $\dot{\boldsymbol{\zeta}}_f$, so that it is possible to express the free twist of the *EE* as a linear combination of the columns of $\mathbf{\Xi}^\perp$, with the combination coefficients $\mathbf{c}$ being the components $\dot{\boldsymbol{\zeta}}_f$. The choice of the permutation matrix $\mathbf{P}$, and subsequently of the free pose components, is not arbitrary, since it must ensure rank$(\mathbf{D}_d) = n$. However, this choice does not need to be unique throughout the robot workspace, but it can be changed locally in order to avoid representation singularities: this is always possible, because rank$(\mathbf{D}) \geq 5$. In addition, in case a direct-kinematics singularity is encountered in the workspace, so that rank$(\mathbf{\Xi}) = n'$, with $n' < n$, the method proposed in this Section for the

---

[1] A permutation matrix is an orthogonal matrix that has exactly one entry of 1 in each row and each column, and has 0's elsewhere [27].

description of the free motion may still be employed: the *DoFs* preserved by the *EE* would be $\lambda' = 6 - n'$, and λ' free pose coordinates and n' dependent pose coordinates could be chosen.

B. FREE-MOTION DYNAMICS

The non-linear dynamic model of an *UACDPR* emerges from the *EE* mechanical equilibrium, subject to cable constraints, inertial actions, and an external wrench [1]:

$$\mathbf{M}\dot{\mathbf{v}} + \mathbf{C}\mathbf{v} = -\mathbf{\Xi}^T\boldsymbol{\tau} + \mathbf{f} \tag{24}$$

$$
\begin{aligned}
\mathbf{M} &\triangleq \begin{bmatrix} m\mathbf{I}_{3\times3} & -m\tilde{\mathbf{s}}' \\ m\tilde{\mathbf{s}}' & \mathbf{I}_P \end{bmatrix}, \quad \mathbf{I}_P \triangleq \mathbf{I}_G - m\tilde{\mathbf{s}}'\tilde{\mathbf{s}}' \\
\mathbf{C} &\triangleq \begin{bmatrix} \mathbf{0}_{3\times3} & -m\tilde{\boldsymbol{\omega}}\tilde{\mathbf{s}}' \\ \mathbf{0}_{3\times3} & \tilde{\boldsymbol{\omega}}\mathbf{I}_P \end{bmatrix}, \quad \mathbf{f} \triangleq \begin{bmatrix} \boldsymbol{\phi} \\ \tilde{\mathbf{q}}'\boldsymbol{\phi} + \boldsymbol{\mu} \end{bmatrix}
\end{aligned}
\tag{25}
$$

where m is the *EE* mass, $\mathbf{I}_G$ is the *EE* inertia tensor about its center of mass G expressed in the inertial frame, the symbol $\sim$ over a vector denotes its skew-symmetric representation, and $\boldsymbol{\tau} \in \mathbb{R}^n$ is an array containing the cable tension magnitudes. $\mathbf{f} \in \mathbb{R}^6$ is a generic external wrench, resulting from a force $\boldsymbol{\phi}$ applied in point Q and a moment $\boldsymbol{\mu}$ directed along $\boldsymbol{\phi}$ (Fig. 1a). Vectors $\mathbf{s}'$ and $\mathbf{q}'$ point from P to G and Q, respectively.

Since the natural oscillation frequencies characterize the free motion of the *EE* about equilibria ($\mathbf{l} = \mathbf{l}_0$, $\dot{\mathbf{l}} = \ddot{\mathbf{l}} = \mathbf{0}_{n\times1}$), it is useful to express (24) in terms of the λ *DoFs* that the *EE* preserves and their derivatives, $\boldsymbol{\zeta}_f, \dot{\boldsymbol{\zeta}}_f, \ddot{\boldsymbol{\zeta}}_f$. This is achieved by considering (2) for $i = 1, \cdots, n$ and a fixed $\mathbf{l}_0$, as well as (23) and its time derivative:

$$\boldsymbol{\zeta} = \boldsymbol{\zeta}(\mathbf{l}_0, \boldsymbol{\zeta}_f), \quad \mathbf{v} = \mathbf{\Xi}^\perp\dot{\boldsymbol{\zeta}}_f, \quad \dot{\mathbf{v}} = \dot{\mathbf{\Xi}}^\perp\dot{\boldsymbol{\zeta}}_f + \mathbf{\Xi}^\perp\ddot{\boldsymbol{\zeta}}_f \tag{26}$$

where $\dot{\mathbf{\Xi}}^\perp$, as any first-order time derivative, is linearly dependent from $\dot{\boldsymbol{\zeta}}_f$ and can be symbolically computed by differentiating the right-hand side of (23) w.r.t. time. The *free motion* internal dynamics of the *EE* can be obtained by substituting (26) in (24) and left-multiplying by $\mathbf{\Xi}^{\perp^T}$. Since $\mathbf{\Xi}^{\perp^T}\mathbf{\Xi}^T = \mathbf{0}_{\lambda\times n}$, then:

$$\mathbf{M}^\perp(\boldsymbol{\zeta}_f)\ddot{\boldsymbol{\zeta}}_f + \mathbf{C}^\perp(\boldsymbol{\zeta}_f, \dot{\boldsymbol{\zeta}}_f)\dot{\boldsymbol{\zeta}}_f - \mathbf{f}^\perp(\boldsymbol{\zeta}_f) = \mathbf{0}_{\lambda\times1} \tag{27}$$

where:

$$\mathbf{M}^\perp \triangleq \mathbf{\Xi}^{\perp^T}\mathbf{M}\mathbf{\Xi}^\perp, \quad \mathbf{C}^\perp \triangleq \mathbf{\Xi}^{\perp^T}\left(\mathbf{M}\dot{\mathbf{\Xi}}^\perp + \mathbf{C}\mathbf{\Xi}^\perp\right),$$
$$\mathbf{f}^\perp \triangleq \mathbf{\Xi}^{\perp^T}\mathbf{f} \tag{28}$$

C. FREE MOTION STIFFNESS

An equilibrium configuration is a set $(\boldsymbol{\zeta}, \mathbf{l}) = (\boldsymbol{\zeta}_0, \mathbf{l}_0)$ such that (2), for $i = 1, \cdots, n$, and (27) are satisfied for $\dot{\boldsymbol{\zeta}}_f = \ddot{\boldsymbol{\zeta}}_f = \mathbf{0}_{\lambda\times1}$, and $\boldsymbol{\tau}$ is element-wise strictly positive [6].

After equilibrium is altered, the restoring action that pushes the system back towards the equilibrium is due to the external wrench and the cable constraint forces. These restoring actions generate the *Free-Motion Stiffness* (*FMS*) $\mathbf{K}^\perp \triangleq -\partial\mathbf{f}^\perp/\partial\boldsymbol{\zeta}_f \in \mathbb{R}^{\lambda\times\lambda}$ of the *UACDPR*.[2]

[2]Please refer to the Appendix for additional details about the tensor notation used in this paper.

The *FMS* was implicitly formulated for UACDPRs in [8], under the assumptions that cables exit the frame through eyelets, and the platform is subject to the gravitational action only, and explicitly formulated accounting for pulley kinematics in [9]. Here, $\mathbf{K}^\perp$ is formulated as in [9], but the application of a generic external wrench $\mathbf{f}$ on the platform is also considered.

According to (22) ($\dot{\boldsymbol{\zeta}} = \mathbf{J}^\perp\dot{\boldsymbol{\zeta}}_f$), one can infer:

$$\mathbf{J}^\perp = \partial\boldsymbol{\zeta}/\partial\boldsymbol{\zeta}_f \tag{29}$$

Thus, accounting for (28):

$$\mathbf{K}^\perp = -\frac{\partial\mathbf{f}^\perp}{\partial\boldsymbol{\zeta}_f} = -\frac{\partial\mathbf{f}^\perp}{\partial\boldsymbol{\zeta}}\mathbf{J}^\perp = -\left(\frac{\partial\mathbf{\Xi}^{\perp^T}}{\partial\boldsymbol{\zeta}}\mathbf{f} + \mathbf{\Xi}^{\perp^T}\frac{\partial\mathbf{f}}{\partial\boldsymbol{\zeta}}\right)\mathbf{J}^\perp \tag{30}$$

Since the restoring actions under examination are those around equilibrium configurations, $\mathbf{f} = \mathbf{\Xi}^T\boldsymbol{\tau}$ (see (24)), and thus:

$$\mathbf{K}_0^\perp = -\left(\frac{\partial\mathbf{\Xi}^{\perp^T}}{\partial\boldsymbol{\zeta}}\mathbf{\Xi}^T\boldsymbol{\tau} + \mathbf{\Xi}^{\perp^T}\frac{\partial\mathbf{f}}{\partial\boldsymbol{\zeta}}\right)\mathbf{J}^\perp \tag{31}$$

where the subscript 0 denotes that $\mathbf{K}_0^\perp$ is calculated in the equilibrium configuration. Differentiating $\mathbf{\Xi}^{\perp^T}\mathbf{\Xi}^T = \mathbf{0}_{\lambda\times n}$ and substituting in (31) yields:

$$\mathbf{K}_0^\perp = \mathbf{\Xi}^{\perp^T}\left(\frac{\partial\mathbf{\Xi}^T}{\partial\boldsymbol{\zeta}}\boldsymbol{\tau} - \frac{\partial\mathbf{f}}{\partial\boldsymbol{\zeta}}\right)\mathbf{J}^\perp \tag{32}$$

The first term in the parentheses at the right-hand side of (32) may be calculated by considering the right-hand side of (5):

$$\frac{\partial\mathbf{\Xi}^T}{\partial\boldsymbol{\zeta}}\boldsymbol{\tau} = \sum_{i=1}^{n}\tau_i\frac{\partial\boldsymbol{\xi}_i}{\partial\boldsymbol{\zeta}} = \sum_{i=1}^{n}\tau_i\begin{bmatrix} \frac{\partial\mathbf{t}_i}{\partial\boldsymbol{\zeta}} \\ \tilde{\mathbf{a}}_i'\frac{\partial\mathbf{t}_i}{\partial\boldsymbol{\zeta}} - \tilde{\mathbf{t}}_i\frac{\partial\mathbf{a}_i'}{\partial\boldsymbol{\zeta}} \end{bmatrix} \tag{33}$$

According to [1], it can be shown by computation that:

$$\frac{\partial\mathbf{t}_i}{\partial\boldsymbol{\zeta}} = \begin{bmatrix} \mathbf{T}_i & -\mathbf{T}_i\tilde{\mathbf{a}}_i' \end{bmatrix}\mathbf{D}, \qquad \mathbf{T}_i \triangleq \frac{\sin\psi_i\mathbf{w}_i\mathbf{w}_i^T}{\mathbf{u}_i\cdot(\mathbf{a}_i - \mathbf{d}_i)} + \frac{\mathbf{n}_i\mathbf{n}_i^T}{\|\boldsymbol{\rho}_i\|} \tag{34}$$

$$\frac{\partial\mathbf{a}_i'}{\partial\boldsymbol{\zeta}} = \begin{bmatrix} \mathbf{0}_{3\times3} & -\tilde{\mathbf{a}}_i' \end{bmatrix}\mathbf{D} \tag{35}$$

thus obtaining:

$$\frac{\partial\mathbf{\Xi}^T}{\partial\boldsymbol{\zeta}}\boldsymbol{\tau} = \mathbf{K}\mathbf{D} \tag{36}$$

with:

$$\mathbf{K} \triangleq \sum_{i=1}^{n}\tau_i\begin{bmatrix} \mathbf{T}_i & -\mathbf{T}_i\tilde{\mathbf{a}}_i' \\ \tilde{\mathbf{a}}_i'\mathbf{T}_i & -\tilde{\mathbf{a}}_i'\mathbf{T}_i\tilde{\mathbf{a}}_i' \end{bmatrix} + \sum_{i=1}^{n}\tau_i\begin{bmatrix} \mathbf{0}_{3\times3} & \mathbf{0}_{3\times3} \\ \mathbf{0}_{3\times3} & \tilde{\mathbf{t}}_i\tilde{\mathbf{a}}_i' \end{bmatrix} \tag{37}$$

In the literature, the (6×6) matrix $\mathbf{K}$ is referred to as *Geometric* [24], *Controllable* [28] or *Active* [29] *Stiffness* of the *CDPR*, because it is geometry dependent and, in over-constrained *CDPRs*, $\boldsymbol{\tau}$ can be actively controlled independently from the *EE* configuration. It should be noted that its definition is fundamentally different from the so-called *Passive Stiffness* generated by cable deformations (not considered in this paper, since cables are modelled as rigid). However, in *UACDPRs*, $\mathbf{K}$ cannot be actively

controlled, because $\boldsymbol{\tau}$ depends on the equilibrium configuration.

The second term in the parentheses at the right-hand side of (32) is calculated from (25). Since $\mathbf{q}' = \mathbf{R}^P\mathbf{q}'$, with $\mathbf{R}$ being the rotation matrix between the moving and the inertial frame, and $^P\mathbf{q}'$ being the coordinates of $\mathbf{q}'$ expressed in $Px'y'z'$, one has:

$$-\frac{\partial \mathbf{f}}{\partial \boldsymbol{\zeta}} = \mathbf{Q}\mathbf{D} - \mathbf{F} \tag{38}$$

$$\mathbf{Q} \triangleq \begin{bmatrix} \mathbf{0}_{3\times3} & \mathbf{0}_{3\times3} \\ \mathbf{0}_{3\times3} & -\tilde{\boldsymbol{\phi}}_i\tilde{\mathbf{q}}'_i \end{bmatrix}, \qquad \mathbf{F} \triangleq \begin{bmatrix} \frac{\partial\boldsymbol{\phi}}{\partial\boldsymbol{\zeta}} \\ \mathbf{R}\frac{\partial^P\mathbf{q}'}{\partial\boldsymbol{\zeta}} + \tilde{\mathbf{q}}'\frac{\partial\boldsymbol{\phi}}{\partial\boldsymbol{\zeta}} + \frac{\partial\boldsymbol{\mu}}{\partial\boldsymbol{\zeta}} \end{bmatrix} \tag{39}$$

since $\partial\mathbf{q}'/\partial\boldsymbol{\zeta} = [\mathbf{0}_{3\times3} \ -\tilde{\mathbf{q}}'_i\mathbf{D} + \mathbf{R}\frac{\partial^P\mathbf{q}'}{\partial\boldsymbol{\zeta}}]$. Finally, substituting (36) and (38) in (32), yields:

$$\mathbf{K}_0^{\perp} = \boldsymbol{\Xi}^{\perp^T}[(\mathbf{K}+\mathbf{Q})\,\mathbf{D} - \mathbf{F}]\,\mathbf{J}^{\perp} \tag{40}$$

where:

$$\mathbf{K}+\mathbf{Q} = \sum_{i=1}^{n}\tau_i\begin{bmatrix} \mathbf{T}_i & -\mathbf{T}_i\tilde{\mathbf{a}}'_i \\ \tilde{\mathbf{a}}'_i\mathbf{T}_i & -\tilde{\mathbf{a}}'_i\mathbf{T}_i\tilde{\mathbf{a}}'_i \end{bmatrix} + $$
$$+ \sum_{i=1}^{n}\tau_i\begin{bmatrix} \mathbf{0}_{3\times3} & \mathbf{0}_{3\times3} \\ \mathbf{0}_{3\times3} & -\tilde{\mathbf{t}}_i\tilde{\mathbf{a}}'_i \end{bmatrix} + \begin{bmatrix} \mathbf{0}_{3\times3} & \mathbf{0}_{3\times3} \\ \mathbf{0}_{3\times3} & \tilde{\boldsymbol{\phi}}_i\tilde{\mathbf{q}}'_i \end{bmatrix} \tag{41}$$

Notice that matrix $\mathbf{K}+\mathbf{Q}$ is generally non-symmetric, since, while the first summation in (41) is always symmetric, the other terms are not. In fact, at the static equilibrium:

$$\sum_{i=1}^{n}\tau_i\mathbf{a}'_i\times\mathbf{t}_i = \mathbf{q}'_i\times\boldsymbol{\phi} + \boldsymbol{\mu} \tag{42}$$

which, in skew-symmetric representation, is equivalent to:

$$\sum_{i=1}^{n}\tau_i\left(\tilde{\mathbf{a}}'_i\tilde{\mathbf{t}}_i - \tilde{\mathbf{t}}_i\tilde{\mathbf{a}}'_i\right) = \tilde{\mathbf{q}}'\tilde{\boldsymbol{\phi}} - \tilde{\boldsymbol{\phi}}\tilde{\mathbf{q}}' + \tilde{\boldsymbol{\mu}} \tag{43}$$

Equation (43) shows that the summation of the second and third term in (41), namely,

$$\tilde{\boldsymbol{\phi}}\tilde{\mathbf{q}}' - \sum_{i=1}^{n}\tau_i\tilde{\mathbf{t}}_i\tilde{\mathbf{a}}'_i = \tilde{\mathbf{q}}'\tilde{\boldsymbol{\phi}} - \sum_{i=1}^{n}\tau_i\tilde{\mathbf{a}}'_i\tilde{\mathbf{t}}_i + \tilde{\boldsymbol{\mu}} = $$
$$= \left(\tilde{\boldsymbol{\phi}}\tilde{\mathbf{q}}' - \sum_{i=1}^{n}\tau_i\tilde{\mathbf{t}}_i\tilde{\mathbf{a}}'_i\right)^T + \tilde{\boldsymbol{\mu}} \tag{44}$$

is symmetric if and only if $\boldsymbol{\mu} = \mathbf{0}_{3\times1}$. If, furthermore, the force $\boldsymbol{\phi}$ is constant, then $\mathbf{F} = \mathbf{0}_{6\times6}$ and the *FMS* is symmetric for *any* choice of *EE* pose parameters (both $\mathbf{p}$ and $\boldsymbol{\epsilon}$):

$$\mathbf{K}_0^{\perp} = \boldsymbol{\Xi}^{\perp^T}(\mathbf{K}+\mathbf{Q})\,\boldsymbol{\Xi}^{\perp} \tag{45}$$

IV. LINEARIZED FREE-MOTION DYNAMICS AND NATURAL OSCILLATIONS

The *UACDPR* natural oscillation frequencies can be computed from the eigenvalue problem arising from the *EE* free-motion dynamics, after its linearization about an equilibrium configuration. A linearized form of (27) can be obtained by expanding it in Taylor series and truncating the expansion at the first order (an example of application to the linearization of the dynamic model of fully-actuated parallel manipulators can be found in [30]). In the following, an approach similar to [30] is followed, but the *EE* coordinates are not considered independent from each other (cf. (22)), which is a distinctive feature of underactuated mechanisms.

If the left-hand side of (27) is denoted by $\mathbf{h}\left(\boldsymbol{\zeta}_f, \dot{\boldsymbol{\zeta}}_f, \ddot{\boldsymbol{\zeta}}_f\right)$, the Taylor-series expansion of (27) about an equilibrium configuration $(\boldsymbol{\zeta}_f = \boldsymbol{\zeta}_{f0}, \ \dot{\boldsymbol{\zeta}}_f = \mathbf{0}_{\lambda\times1}, \ \ddot{\boldsymbol{\zeta}}_f = \mathbf{0}_{\lambda\times1})$ truncated at the first order yields:

$$\mathbf{h}\left(\boldsymbol{\zeta}_f, \dot{\boldsymbol{\zeta}}_f, \ddot{\boldsymbol{\zeta}}_f\right) \simeq \mathbf{h}\left(\boldsymbol{\zeta}_{f0}, \mathbf{0}, \mathbf{0}\right) + \left.\frac{\partial\mathbf{h}}{\partial\ddot{\boldsymbol{\zeta}}_f}\right|_{(\boldsymbol{\zeta}_{f0},\mathbf{0},\mathbf{0})}\ddot{\boldsymbol{\zeta}}_f + $$
$$+ \left.\frac{\partial\mathbf{h}}{\partial\dot{\boldsymbol{\zeta}}_f}\right|_{(\boldsymbol{\zeta}_{f0},\mathbf{0},\mathbf{0})}\dot{\boldsymbol{\zeta}}_f + \left.\frac{\partial\mathbf{h}}{\partial\boldsymbol{\zeta}_f}\right|_{(\boldsymbol{\zeta}_{f0},\mathbf{0},\mathbf{0})}\left(\boldsymbol{\zeta}_f - \boldsymbol{\zeta}_{f0}\right) = \mathbf{0}_{\lambda\times1} \tag{46}$$

At equilibrium, $\mathbf{h}\left(\boldsymbol{\zeta}_{f0}, \mathbf{0}, \mathbf{0}\right) = \mathbf{f}^{\perp} = \mathbf{0}_{\lambda\times1}$. The partial derivatives are readily obtained as:

$$\left.\frac{\partial\mathbf{h}}{\partial\ddot{\boldsymbol{\zeta}}_f}\right|_{(\boldsymbol{\zeta}_{f0},\mathbf{0},\mathbf{0})} = \mathbf{M}^{\perp}\big|_{(\boldsymbol{\zeta}_{f0},\mathbf{0},\mathbf{0})} = \mathbf{M}_0^{\perp} \tag{47}$$

$$\left.\frac{\partial\mathbf{h}}{\partial\dot{\boldsymbol{\zeta}}_f}\right|_{(\boldsymbol{\zeta}_{f0},\mathbf{0},\mathbf{0})} = \left.\left(\mathbf{C}^{\perp} + \frac{\partial\mathbf{C}^{\perp}}{\partial\dot{\boldsymbol{\zeta}}_f}\dot{\boldsymbol{\zeta}}_f\right)\right|_{(\boldsymbol{\zeta}_{f0},\mathbf{0},\mathbf{0})} = \mathbf{0}_{\lambda\times\lambda} \tag{48}$$

$$\left.\frac{\partial\mathbf{h}}{\partial\boldsymbol{\zeta}_f}\right|_{(\boldsymbol{\zeta}_{f0},\mathbf{0},\mathbf{0})} = \left.\left(\frac{\partial\mathbf{M}^{\perp}}{\partial\boldsymbol{\zeta}_f}\ddot{\boldsymbol{\zeta}}_f + \frac{\partial\mathbf{C}^{\perp}}{\partial\boldsymbol{\zeta}_f}\dot{\boldsymbol{\zeta}}_f - \frac{\partial\mathbf{f}^{\perp}}{\partial\boldsymbol{\zeta}_f}\right)\right|_{(\boldsymbol{\zeta}_{f0},\mathbf{0},\mathbf{0})} = $$
$$= -\left.\frac{\partial\mathbf{f}^{\perp}}{\partial\boldsymbol{\zeta}_f}\right|_{(\boldsymbol{\zeta}_{f0},\mathbf{0},\mathbf{0})} = \mathbf{K}^{\perp}\big|_{(\boldsymbol{\zeta}_{f0},\mathbf{0},\mathbf{0})} = \mathbf{K}_0^{\perp} \tag{49}$$

where many elements vanishing in (47), (48) and (49) are linearly dependent on $\dot{\boldsymbol{\zeta}}_f$ and $\ddot{\boldsymbol{\zeta}}_f$ (and thus are naught), and matrices $\mathbf{M}_0^{\perp}$ and $\mathbf{K}_0^{\perp}$, given in (28) and (40), are reported below for the sake of convenience:

$$\mathbf{M}_0^{\perp} = \boldsymbol{\Xi}^{\perp^T}\mathbf{M}\boldsymbol{\Xi}^{\perp} \tag{50}$$

$$\mathbf{K}_0^{\perp} = \boldsymbol{\Xi}^{\perp^T}[(\mathbf{K}+\mathbf{Q})\,\mathbf{D} - \mathbf{F}]\,\mathbf{J}^{\perp} \tag{51}$$

All quantities at the right-hand sides of (50) and (51) are intended to be computed in the equilibrium configuration.

Finally, (46) can be rewritten as:

$$\mathbf{M}_0^{\perp}\ddot{\boldsymbol{\zeta}}_f + \mathbf{K}_0^{\perp}\left(\boldsymbol{\zeta}_f - \boldsymbol{\zeta}_{f0}\right) = \mathbf{M}_0^{\perp}\Delta\ddot{\boldsymbol{\zeta}}_{f0} + \mathbf{K}_0^{\perp}\Delta\boldsymbol{\zeta}_{f0} = \mathbf{0}_{\lambda\times1} \tag{52}$$

where $\Delta\ddot{\boldsymbol{\zeta}}_{f0} \triangleq \ddot{\boldsymbol{\zeta}}_f - \mathbf{0}_{\lambda\times1}$ and $\Delta\boldsymbol{\zeta}_{f0} \triangleq \boldsymbol{\zeta}_f - \boldsymbol{\zeta}_{f0}$.

This formulation leads to a generalized eigenvalue problem, whose solution allows for the determination of the system natural oscillation frequencies in the equilibrium configuration under investigation. By considering a solution of (52) in the form $\Delta\boldsymbol{\zeta}_{f0}(t) = \boldsymbol{\gamma}e^{\Lambda t}$, with $\Lambda \in \mathbb{C}$, so that:

$$\left(\Lambda^2\mathbf{M}_0^{\perp} + \mathbf{K}_0^{\perp}\right)\boldsymbol{\gamma} = \mathbf{0}_{\lambda\times1} \tag{53}$$

i	1	2	3	4
$\mathbf{d}_i$ [m]	$\begin{bmatrix} 0.219 \\ -1.316 \\ 0.527 \end{bmatrix}$	$\begin{bmatrix} 2.295 \\ -1.158 \\ 0.521 \end{bmatrix}$	$\begin{bmatrix} 2.153 \\ 0.973 \\ 0.560 \end{bmatrix}$	$\begin{bmatrix} 0.0532 \\ 0.796 \\ 0.532 \end{bmatrix}$
r_i [m]	0.025	0.025	0.025	0.025
$^P\mathbf{a}_i'$ [m]	$\begin{bmatrix} -0.144 \\ -0.219 \\ 0.264 \end{bmatrix}$	$\begin{bmatrix} 0.115 \\ -0.233 \\ 0.270 \end{bmatrix}$	$\begin{bmatrix} 0.142 \\ 0.220 \\ 0.266 \end{bmatrix}$	$\begin{bmatrix} -0.120 \\ 0.236 \\ 0.266 \end{bmatrix}$
$\mathbf{x}_i$	$\mathbf{j}$	$-\mathbf{i}$	$-\mathbf{j}$	$\mathbf{i}$
$\mathbf{y}_i$	$-\mathbf{k}$	$-\mathbf{k}$	$-\mathbf{k}$	$-\mathbf{k}$
$\mathbf{z}_i$	$-\mathbf{i}$	$-\mathbf{j}$	$\mathbf{i}$	$\mathbf{j}$

Table 1: Actuators' properties

m [Kg]	$^P\mathbf{I}_G$ [Kg·m²]			$^P\mathbf{s}'$ [m]
8	$\begin{bmatrix} 0.1338 & 0.0059 & 0.0021 \\ 0.0059 & 0.1814 & -0.0055 \\ 0.0021 & -0.0055 & 0.2602 \end{bmatrix}$			$\begin{bmatrix} 0.002 \\ -0.002 \\ 0.200 \end{bmatrix}$

Table 2: Platform inertial properties

the eigenvalues $\Lambda_1^2,\ldots,\Lambda_\lambda^2$ are found by solving the characteristic equation, namely:

$$\det\left(\Lambda^2 \mathbf{M}_0^\perp + \mathbf{K}_0^\perp\right) = 0 \qquad (54)$$

Based on (54), it is possible to define the stability conditions of a *UACDPR* equilibrium configuration: if and only if $\Lambda_1^2,\ldots,\Lambda_\lambda^2$ are real negative numbers, *the equilibrium configuration is stable, otherwise it is unstable* [31]. When $\mathbf{K}_0^\perp$ is symmetric (and only in this case), the latter assertion is equivalent to requiring $\mathbf{K}_0^\perp$ to be positive-definite [8]. Finally, natural oscillation frequencies are computed (in [Hz]) as:

$$f_j = \frac{\Im\left(\Lambda_j\right)}{2\pi} \qquad (55)$$

where $\Im(\cdot)$ denotes the imaginary part of a complex number. Additionally, eigenvectors $\boldsymbol{\gamma}_j$ can be determined by solving (53) for each j and normalized according to $\boldsymbol{\gamma}_j^T \mathbf{M}_0^\perp \boldsymbol{\gamma}_j = 1$.

V. EXPERIMENTAL VALIDATION

In order to validate the methodology proposed in this paper, a series of experiments were conducted on the 6-*DoF UACDPR* prototype of the University of Bologna (Fig. 2). Geometrical and inertial properties of the prototype are deduced from the prototype *CAD* models, and are summarized in Tables 1 and 2, where $\mathbf{i} = [1;0;0]^T$, $\mathbf{j} = [0;1;0]^T$, and $\mathbf{k} = [0;0;1]^T$, and the only external load applied to the robot *EE* is gravity, thus $\mathbf{q}' = \mathbf{s}'$, $\boldsymbol{\phi} = -mg\mathbf{k}$ and $\boldsymbol{\mu} = \mathbf{0}_{3\times 3}$. The coordinates of $\mathbf{a}_i'$, $\mathbf{s}'$ and $\mathbf{I}_G$ are constant
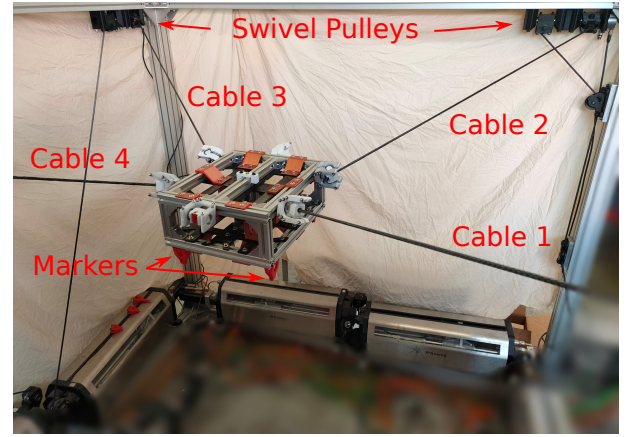

Figure 2: *UACDPR Prototype*

in the *EE* frame, and denoted as $^P\mathbf{a}_i'$, $^P\mathbf{s}'$ and $^P\mathbf{I}_G$ in $Px'y'z'$.

A. EXPERIMENTAL METHODOLOGY

The procedure described in this Section was applied to, respectively: 30 equilibrium configurations in which the platform was constrained by 4 cables (cables 1 to 4, Fig. 3a), 30 configurations in which only cables 1 through 3 were attached to the platform (Fig. 3b), and 30 configurations in which the platform was only suspended by cables 1 and 3 (Fig. 3c).

Each equilibrium configuration was reached by quasi-statically varying robot cable lengths; once the assigned set-point was reached, actuators were controlled to hold their angular positions so that cable lengths could not vary any longer, and motor torques were checked to ensure that their values were compatible with cables being taut. The *EE* was then manually slightly displaced w.r.t. its equilibrium configuration, and swiftly released next: this operation was equivalent to impose non-equilibrium initial conditions to the free-motion dynamics of the platform. The positions $\mathbf{p}_k$, $k = 1,\ldots,5$, of 5 optical markers mounted on the robot platform (2 of which can be seen in Fig. 2) were tracked by 8 cameras of a VICON Motion Capture System (measurement accuracy was ±0.2 mm for each marker's Cartesian component, at a 100 Hz sampling rate) for a total duration of 10 s for each experiment, thus acquiring $n_s = 1001$ samples per marker coordinate.

These coordinates were then filtered by using a zero-phase finite-impulse response low-pass digital filter with a stop-band frequency of 10 Hz. No natural oscillation frequency above 4 Hz was expected from the model, thus measurement noise and unmodelled oscillatory phenomena at higher frequencies, such as cable elastic axial vibrations, were accordingly removed.

For each experiment, the n_s *EE* poses recorded during oscillations were reconstructed from the position of the 5 markers, and the corresponding cable lengths were calculated by the inverse geometric model (see (2)). The
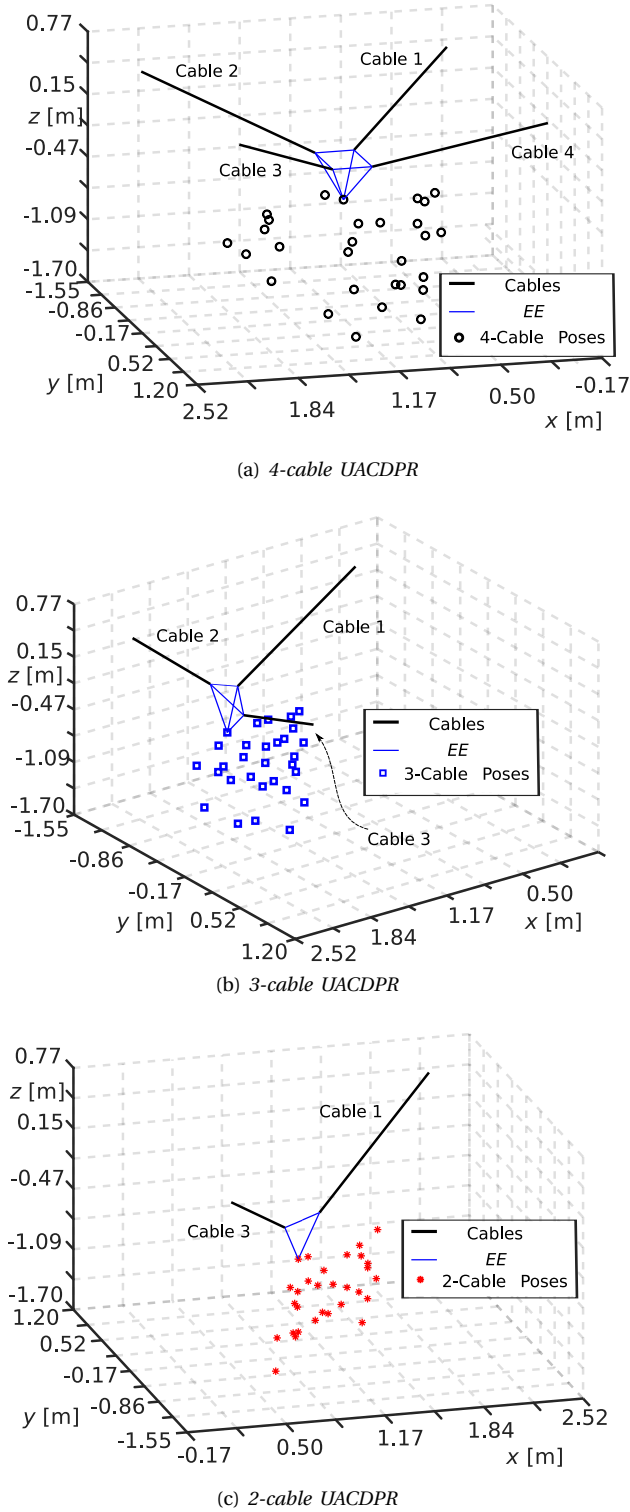
(a) *4-cable UACDPR*

(b) *3-cable UACDPR*

(c) *2-cable UACDPR*

Figure 3: *Layout of experimental configurations*

mean value over the n_s samples of each cable length differed from its maximum and minimum value by less than 1 mm and thus it was considered as the constant experimental value of the variable $\mathbf{l}_0^\star$. Alternatively, cable

lengths could be computed as the result of the inverse model applied to the rest pose of the *EE* that is eventually reached. On the other hand, the employed procedure is considered to be more robust, because static friction may lead the *EE* to stop in a configuration different from the theoretical one.

The natural-oscillation-frequency computation method proposed is summarized as follows:

- given the experimental value $\mathbf{l}_0^\star$ of cable lengths, compute the corresponding *EE* static equilibrium pose $\boldsymbol{\zeta}_0^\star$ according to the direct geometric-static model [6] ($\boldsymbol{\epsilon}$ is expressed by xyz Tait-Bryan angles); since the problem has possibly multiple solutions, keep only the stable pose that is closer to the initial one;
- once the equilibrium configuration $(\boldsymbol{\zeta}_0^\star, \mathbf{l}_0^\star)$ is known, compute $\mathbf{M}_0^\perp$ and $\mathbf{K}_0^\perp$ according to (50) and (51);
- solve the generalized eigenvalue problem in (53) and compute the natural oscillation frequencies f_j, for $j = 1, \ldots, \lambda$, according to (55).

The experimental value $f_j^\star$ of each *EE* natural oscillation frequency was then identified, for $j = 1, \ldots, \lambda$, from the marker recorded positions, so that a comparison with the corresponding modelled value f_j could be performed. The oscillation of each marker w.r.t. its equilibrium position was experimentally computed as:

$$\Delta \mathbf{p}_k(t) = \mathbf{p}_k(t) - \overline{\mathbf{p}}_k \qquad (56)$$

where $(\overline{\cdot})$ denotes the mean value operator. The signal of any coordinate of $\Delta \mathbf{p}_k(t)$ contains, in general, the system natural frequencies since, if $\mathbf{p}_k$ is chosen as the platform reference point, $\Delta \mathbf{p}_k(t)$ can be modelled as:

$$\Delta \mathbf{p}_k(t) = \mathbf{J}_k^\perp \Delta \boldsymbol{\zeta}_{f0}(t) = \mathbf{J}_k^\perp \boldsymbol{\gamma} e^{\Lambda t} = \boldsymbol{\gamma}_k e^{\Lambda t}, \qquad \boldsymbol{\gamma}_k \triangleq \mathbf{J}_k^\perp \boldsymbol{\gamma} \quad (57)$$

where $\mathbf{J}_k^\perp$ groups the first 3 rows of $\mathbf{J}^\perp$ as in the left-hand side of (22). Then, the *Fast Fourier Transformation* (*FFT*) of each coordinate of $\Delta \mathbf{p}_k(t)$, for $k = 1, \ldots, 5$, was performed. This operation was deemed necessary since: (i) depending to the actual value of $\boldsymbol{\gamma}_k$, some modes may be absent in some coordinate, (ii) depending on the manually imposed initial condition of the *EE* oscillation, some modes may have an experimentally negligible amplitude in the frequency spectra of a certain coordinate *FFT*, and (iii) high data redundancy, which is achieved by considering 15 signals theoretically possessing frequency spectra peaks corresponding to the same frequency values, robustifies the experimental investigation. Figure 4 shows, as an example, the *FFT*s produced while analyzing experiment 77 on the 2-cable *UACDPR*. Several small-amplitude peaks can be noticed surrounding high amplitude-peaks: they are not present in the original signals, but artificially introduced because of an *FFT* resolution upscaling process. In fact, $n_s = 1001$ samples recorded at 100 Hz would produce an *FFT* with 0.1 Hz frequency resolution. This resolution was upscaled to
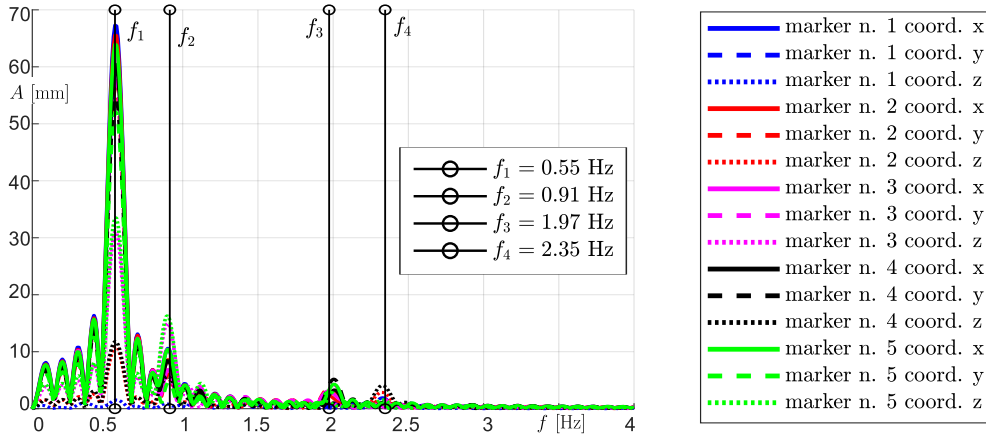
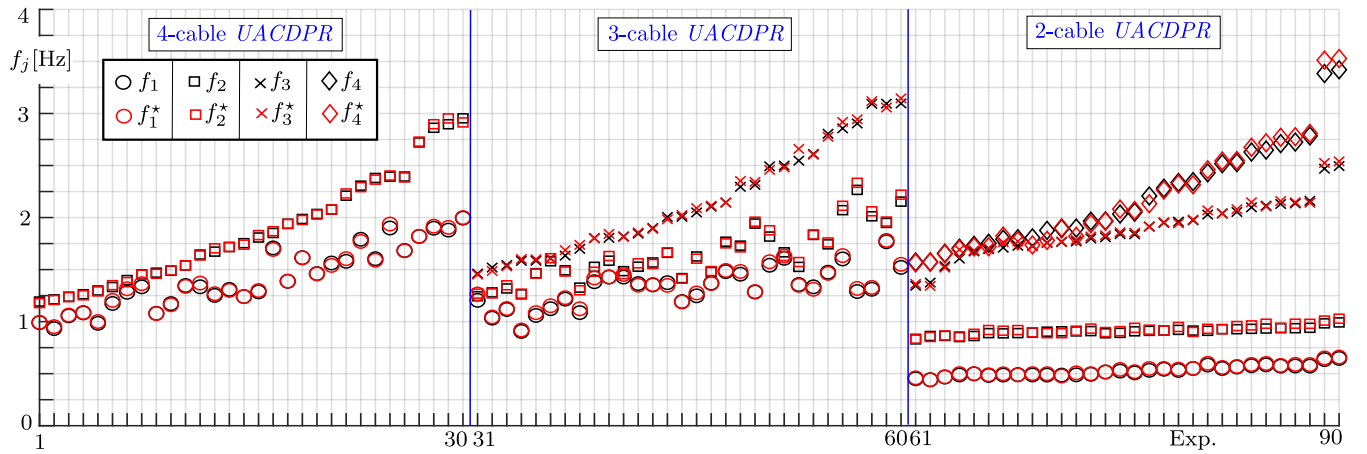Figure 4: *Example of experimental FFTs: experiment 77 on the 2-cable UACDPR*

Figure 5: *Modelled and experimental oscillation frequencies for UACDPRs with 2, 3 and 4 cables.*

0.01 Hz in order to better isolate nearby peaks of the signal *FFT*s. This operation was performed by adding, at the end of the n_s recorded samples, $9n_s$ additional zero-value samples, for a total of $10n_s = 10001$ samples.

B. DISCUSSION OF RESULTS

For each experiment, the experimental natural frequency $f_j^\star$ is determined as the weighted mean of the frequencies $f_{j,kc}^\star$ corresponding to *FFT* peaks of a single coordinate, with the oscillation amplitude A_{kc} used as weight ($k = 1,\dots,5$, $c = x,y,z$):

$$f_j^\star = \left(\sum_{k=1}^{5} \sum_{c=x}^{z} A_{kc} f_{j,kc}^\star \right) \bigg/ \left(\sum_{k=1}^{5} \sum_{c=x}^{z} A_{kc} \right) \quad (58)$$

The results[3] of all experiments are summarized in Fig. 5, where each integer between 1 and 90 on the abscissa axis represents one of the experimental configurations portrayed in Fig. 3, with the ordinate representing the corresponding values of f_j (in black) and $f_j^\star$ (in red), for $j = 1,\dots,\lambda$.

[3]Complete experimental data, and the associated descriptive statics, can be found in [32].

In order to evaluate how different *FFT* peaks corresponding to the same natural frequency are dispersed w.r.t. their mean value, the percentage standard deviation of the weighted mean was analyzed:

$$\sigma_j^\star\% = 100 \sqrt{ \left(\sum_{k=1}^{5} \sum_{c=x}^{z} A_{kc} \left(f_{j,kc}^\star - f_j^\star \right)^2 \right) \bigg/ \left(\sum_{k=1}^{5} \sum_{c=x}^{z} A_{kc} \right) } \quad (59)$$

The smaller $\sigma_j^\star\%$ is, the better the natural frequency is experimentally identified. A descriptive statistics of $\sigma_j^\star\%$ for each mode $j = 1,\dots,\lambda$, organized by architecture (4-, 3-, 2-cable *UACDPRs*), is given in Table 3. Mean values are less than 3% across all modes and architectures, minimum values are below 1% and the largest value is roughly 6%: the proposed frequency-identification method is deemed well performing, especially considering the prototype nature of the robot used in the experiments (most structural components, except for the winches, are made of 3D-printed plastic).

In order to asses how well the experimental natural frequency $f_j^\star$ matches the modelled one f_j, the (absolute)

j	mean($\sigma_j^\star$%)	max($\sigma_j^\star$%)	min($\sigma_j^\star$%)
4-cable *UACDPR*			
1	0.96%	3.18% (Exp. 26)	0.04% (Exp. 7)
2	1.56%	4.21% (Exp. 29)	0.26% (Exp. 9)
3-cable *UACDPR*			
1	2.36%	6.06% (Exp. 46)	0.21% (Exp. 33)
2	1.79%	5.52% (Exp. 42)	0.19% (Exp. 56)
3	1.78%	3.50% (Exp. 35)	0.12% (Exp. 50)
2-cable *UACDPR*			
1	0.70%	2.70% (Exp. 76)	0.09% (Exp. 65)
2	1.34%	3.94% (Exp. 63)	0.25% (Exp. 75)
3	2.28%	4.30% (Exp. 68)	0.53% (Exp. 77)
4	2.87%	4.91% (Exp. 87)	0.29% (Exp. 63)

Table 3: $\sigma_j^\star$% descriptive statistics.

j	mean(Δf_j%)	max(Δf_j%)	min(Δf_j%)
4-cable *UACDPR*			
1	1.07%	2.66% (Exp. 6)	0.09% (Exp. 13)
2	0.70%	1.87% (Exp. 28)	0.04% (Exp. 21)
3-cable *UACDPR*			
1	1.41%	4.45% (Exp. 43)	0.08% (Exp. 42)
2	1.61%	5.05% (Exp. 60)	0.06% (Exp. 49)
3	1.38%	3.10% (Exp. 52)	0.25% (Exp. 32)
2-cable *UACDPR*			
1	1.86%	3.87% (Exp. 80)	0.05% (Exp. 65)
2	2.14%	4.92% (Exp. 73)	0.03% (Exp. 64)
3	1.06%	3.08% (Exp. 78)	0.16% (Exp. 74)
4	1.88%	5.38% (Exp. 77)	0.16% (Exp. 61)

Table 4: Δf_j% descriptive statistics.

percentage estimation error is additionally analyzed:

$$\Delta f_j\% = 100 \left\| \frac{f_j^\star - f_j}{f_j} \right\| \tag{60}$$

A descriptive statistics of Δf_j% for each mode $j = 1, \ldots, \lambda$, organized by architecture (4-, 3-, 2-cable *UACDPRs*), is given in Table 4, where the experiment number matching maximum and minimum statistical indicators is reported within parentheses. Mean values are less than 2.5% across all modes and architectures, minimum errors are below 0.5% and the largest error is less than 6%: it can be ultimately concluded that the proposed method for natural-frequency computation is accurate, in practice. In fact, from an engineering perspective, a mean error of the order of $1-2\%$ is negligible in most applications.

In addition, various error sources, such as an imperfect knowledge of robot geometry and inertial parameters, which were estimated from *CAD* drawings, could also have had a negative impact on the evaluation of the modelled natural frequencies f_j.

It should be noted that, while experimentally studying *UACDPRs* natural frequencies, additional *FFT* small-amplitude peaks, which did not match any phenomena modelled in this paper, were occasionally detected. These additional vibratory/oscillatory phenomena were expected, since cables may vibrate axially or flexurally, or they may oscillate out of the pulley planes. On the other hand, the amplitude of these phenomena (i.e. tenths of a millimeter) is negligible w.r.t. the amplitude of natural oscillations (up to dozens of millimeters, see Fig. 4), for the prototype used in the experimentation. These additional effects will be addressed in our future work on a larger-scale prototype.

VI. APPLICATION EXAMPLE

In order to highlight the interest of the modelling strategy proposed in this paper in a robotic context, a *potential* application example is presented in the following: the trajectory planning of a 6-*DoF* 4-cable *UACDPR* by a frequency-based method (i.e. Multi-Mode Zero-Vibration Input Shaping [16], [22]), experimentally compared with traditional methods. The robot under investigation has $\lambda = 2$ free pose components, and thus the trajectory of 4 *EE* dependent coordinates can be assigned for planning purposes[4]. The natural frequencies of the robot are determined by taking into account the exact 4-cable 6-*DoF* architecture of the robot (an approximated method is reported in [14], which, according its authors, may have limitations when motion is performed near workspace edges).

Three trajectories are compared, in the form:

$$\zeta_d(t) = \zeta_{d,s} + (\zeta_{d,f} - \zeta_{d,s})u(t) \tag{61}$$

with $\zeta_{d,s}$ and $\zeta_{d,f}$ being start and final values of dependent pose coordinates respectively, and $u(0) = 0$, $u(T) = 1$, $0 \leq u(t) \leq 1 \, \forall t$. All trajectories have equal start and final configurations, but they differ in the choice of the motion law $u(t)$, as follows:

- the first motion law, called STD$_T$, is a standard trapezoidal velocity profile, with total transition time T, and αT acceleration and deceleration duration ($0 \leq \alpha \leq 0.5$):

$$u_{\text{STD}_T}(t) = \begin{cases} \frac{(t/T)^2}{2\alpha(1-\alpha)}, & t < \alpha T \\ \frac{(-\alpha + 2t/T)}{2(1-\alpha)}, & \alpha T \leq t \leq (1-\alpha)T \\ \frac{-2\alpha^2 + 2\alpha - 1 + t/T - (t/T)^2}{2\alpha(1-\alpha)}, & t > (1-\alpha)T \end{cases} \tag{62}$$

[4]In the context of trajectory planning, dependent coordinates are also called controlled coordinates, or actuated coordinates [1].
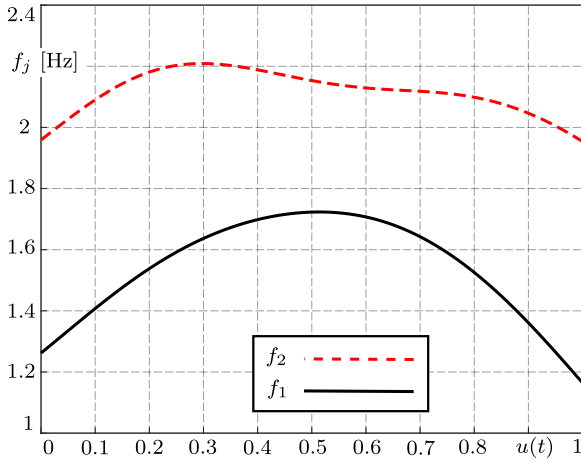
Figure 6: *Modelled oscillation frequencies along $u(t)$.*

- the second motion law, called $\mathrm{STD}_T - \mathrm{IS}$, is the convolution of STD_T with a multi-mode zero-vibration input shaper [22]:

$$u_{\mathrm{STD}_T - \mathrm{IS}}(t) = u_{\mathrm{STD}_T}(t) * S(t) \tag{63}$$

$$S(t) = \sum_{i=1}^{k} A_i \delta_i(t - t_i) \tag{64}$$

where $*$ denotes the convolution operation, $\delta_i(t = t_i) = 1$, $\delta_i(t \neq t_i) = 0$, A_i is the impulse amplitude, t_i is the time at which the impulse occurs, and k is the number of impulses; the convolution with an input-shaper delays the total duration of the trajectory by $\Delta T = t_k$;

- the last motion law, called $\mathrm{STD}_{T+\Delta T}$, is a standard trapezoidal velocity profile, with total transition time $T + \Delta T$, and $\alpha(T + \Delta T)$ acceleration and deceleration duration.

Once a trajectory for the dependent coordinates is assigned, the evolution of the free coordinates when the system is following the prescribed trajectory must be evaluated. Free coordinates are computed by numerically integrating the system internal dynamics, which is obtained by pre-multiplying (24) by $\mathbf{\Xi}^{\perp T}$ and substituting the left-hand side of (3) and (13), and their time derivatives[5]:

$$\mathbf{M}_P \ddot{\boldsymbol{\zeta}}_P + \mathbf{C}_P \dot{\boldsymbol{\zeta}}_P = \mathbf{f}^{\perp} \tag{65}$$

$$\mathbf{M}_P \overset{\Delta}{=} \mathbf{\Xi}^{\perp T} \mathbf{M} \mathbf{D} \mathbf{P}^T = \left[\mathbf{M}_d \, \mathbf{M}_f \right], \, \mathbf{M}_d \in \mathbb{R}^{\lambda \times n}, \mathbf{M}_f \in \mathbb{R}^{\lambda \times \lambda} \tag{66}$$

$$\mathbf{C}_P \overset{\Delta}{=} \mathbf{\Xi}^{\perp T} \left(\mathbf{M} \dot{\mathbf{D}} + \mathbf{C} \mathbf{D} \right) \mathbf{P}^T \tag{67}$$

After algebraic manipulation, the time-derivative of vector $\mathbf{x} \overset{\Delta}{=} \left[\boldsymbol{\zeta}_f^T, \dot{\boldsymbol{\zeta}}_f^T \right]^T$ can be expressed as:

$$\dot{\mathbf{x}} = \begin{bmatrix} \dot{\boldsymbol{\zeta}}_f^T \\ \mathbf{M}_f^{-1} \left(-\mathbf{M}_d \ddot{\boldsymbol{\zeta}}_d - \mathbf{C}_P \dot{\boldsymbol{\zeta}}_P + \mathbf{f}^{\perp} \right) \end{bmatrix} \tag{68}$$

[5]While performing a trajectory, cable lengths change and the elements of $\boldsymbol{\zeta}_P$ and its time derivatives are independent, as opposite to when the *EE* is in free-motion and only $\boldsymbol{\zeta}_f$ and its time derivatives are independent.

and (68) can be numerically integrated for assigned initial rest condition $\mathbf{x}_0$ ($\boldsymbol{\zeta}_{f0}$ is the static equilibrium value for an assigned $\boldsymbol{\zeta}_{d0}$ and $\dot{\boldsymbol{\zeta}}_{f0} = \mathbf{0}_{\lambda}$). Finally, cable lengths can be computed according to the inverse geometric model in (2), and fed to low-level motor drivers for manipulator control. While servo-motor angular positions are closed-loop controlled, there is no feedback on the platform pose, and thus its configuration is only feed-forward controlled.

Start and end configurations are selected near the *UACDPR* static workspace edges [33], in order to stress the importance of careful trajectory planning so as to avoid potentially dangerous situations, such as cable loss of tension due to platform large oscillatory motions. $\boldsymbol{\epsilon}$ is expressed by xyz Tait-Bryan angles, since no representation singularities are expected throughout the manipulator static workspace:

$$\boldsymbol{\zeta}_s = [0.36, -0.82, -0.37, -0.35, 0.51, 0.12]^T \, [\mathrm{m}, \mathrm{rad}]$$
$$\boldsymbol{\zeta}_e = [1.82, 0.55, -0.37, 0.38, -0.25, 0]^T \, [\mathrm{m}, \mathrm{rad}]$$

Natural oscillation frequencies along the path defined by $\boldsymbol{\zeta}_s$ and $\boldsymbol{\zeta}_e$ vary in the range $[1.19, 2.21]$ Hz (see Fig. 6) and can be computed by the method described in Sections III and IV. Since the ratio between the maximum and minimum frequency is almost 2, a convoluted multi-mode zero-vibration Input Shaper with 3 modes is designed: the 4 pairs (A_i, t_i), $i = 1, \ldots, 4$ are determined by setting to zero both summations inside the parentheses of the residual-amplitude equation [16], [22]:

$$A_{\%}(f) = \sqrt{\left(\sum_{i=1}^{k} A_i \cos(2\pi f t_i) \right)^2 + \left(\sum_{i=1}^{k} A_i \sin(2\pi f t_i) \right)^2} \tag{69}$$

for $f = 1.19, \, 1.7, \, 2.21$ Hz (the minimum, mean and maximum frequencies in the range), by considering $t_1 = 0$ s, and imposing $\sum_{i=1}^{k} A_i = 1$; this procedure results in:

$$IS: \quad \begin{array}{l} A_1 = A_4 = 0.1575, \, A_2 = A_3 = 0.3425 \\ t_1 = 0 \, \mathrm{s}, \, t_1 = 0.294 \, \mathrm{s}, \, t_3 = 0.588 \, \mathrm{s}, \, t_4 = 0.882 \, \mathrm{s} \end{array} \tag{70}$$

with $\Delta T = t_4$. Trapezoidal motion law parameters are selected as $\alpha = 0.2$ and $T = 1.5$ s. Finally, dependent components are selected as $\mathbf{p}$ and ϵ_3. While the choice of $\mathbf{p}$ as part of the dependent coordinates is natural if a positioning task has to be performed, no particular strategy is readily available for the choice of orientation parameters as dependent coordinates. For our demonstrative purpose, any choice is suitable: ϵ_3 is chosen due to its limited variation between the start and final configurations.

Complete experiments can be visualized in the media material attached to this paper, and free components ϵ_1 and ϵ_2 time evolution during experiment is shown in Fig. 7 as recorded by the Vicon Camera system described in Sec. V. When comparing trajectories with the same total duration, namely $\mathrm{STD}_T - \mathrm{IS}$ and $\mathrm{STD}_{T+\Delta T}$, it is

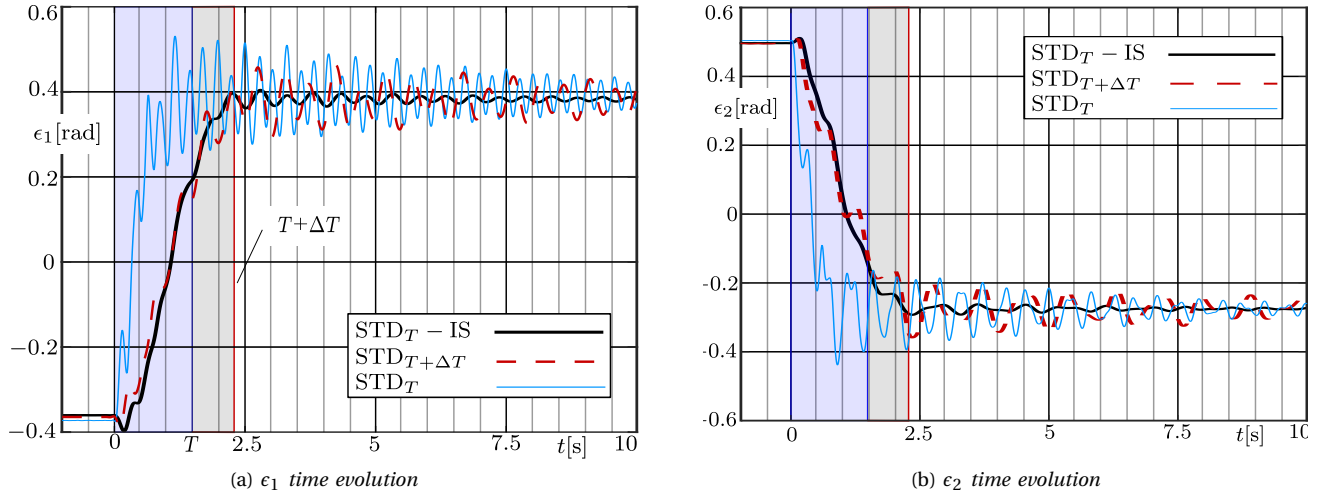(a) ϵ_1 *time evolution*

(b) ϵ_2 *time evolution*

Figure 7: *Free components of the 4-cable UACDPR prototype*

evident that the former allows for smaller amplitude oscillations, which are rapidly damped by unmodelled frictional effects, once the target destination is reached. On the other hand, when comparing unshaped and shaped trajectories, namely STD_T and $\text{STD}_T - \text{IS}$, the advantage in employing the latter is even more evident, since the former results in large platform oscillations not only at the final destination, but also during the transition: this fact could easily lead to platform instability and cable loss of tension, thus ultimately robot loss of control. In the attached video material, it can be easily appreciated a complete loss of tension in cable number 2 during the STD_T trajectory, as well as an overall better tracking performance of the $\text{STD}_T - \text{IS}$ trajectory.

VII. CONCLUSIONS

This paper presented a methodology for the computation of the natural oscillation frequencies of underactuated cable-driven parallel robots. The approach was experimentally validated on 2-,3-, and 4-cable prototypes. According to the experimental data, the method was shown to be effective, because recorded oscillation frequencies deviated from the model less than 6%. As a possible application example, the proposed approach was employed for comparing standard trajectory-planning methods and a frequency-based input-shaping planning of a 4-cable *UACDPR*, resulting in remarkably reduced *EE* residual oscillations even at workspace edges. In the future, this method will be considered for robust calibration and dynamic parameter identification of *UACDPRs*. In addition, cable deformation and sagging will be modelled in order to account for vibrational effects, which may play a role in large-scale *UACDPRs*. Finally, another line of investigation will be the use of different techniques to approximate non-linear systems compared to linearization, such as the method of multiple scales [34]: these techniques

may better describe the system behaviour over large oscillations.

APPENDIX: TENSOR NOTATION

Let:

$$\mathbf{A} \triangleq \begin{bmatrix} \mathbf{a}_1 & \cdots & \mathbf{a}_h \end{bmatrix} \in \mathbb{R}^{k \times h}, \qquad \mathbf{a}_i \triangleq \begin{bmatrix} a_{1i} \\ \vdots \\ a_{ki} \end{bmatrix} \in \mathbb{R}^{k \times 1} \qquad (71)$$

$$\mathbf{b} \triangleq \begin{bmatrix} b_1 \\ \vdots \\ b_h \end{bmatrix} \in \mathbb{R}^{h \times 1}, \qquad \mathbf{c} \triangleq \begin{bmatrix} c_1 \\ \vdots \\ c_l \end{bmatrix} \in \mathbb{R}^{l \times 1} \qquad (72)$$

The derivative of a scalar w.r.t. a vector is:

$$\frac{\partial b_i}{\partial \mathbf{c}} \triangleq \begin{bmatrix} \frac{\partial b_i}{\partial c_1} & \cdots & \frac{\partial b_i}{\partial c_l} \end{bmatrix} \in \mathbb{R}^{1 \times l} \qquad (73)$$

and the derivative of a vector w.r.t. a vector is:

$$\frac{\partial \mathbf{a}_i}{\partial \mathbf{c}} \triangleq \begin{bmatrix} \frac{\partial a_{1i}}{\partial c_1} & \cdots & \frac{\partial a_{1i}}{\partial c_l} \\ \vdots & \ddots & \vdots \\ \frac{\partial a_{ki}}{\partial c_1} & \cdots & \frac{\partial a_{ki}}{\partial c_l} \end{bmatrix} \in \mathbb{R}^{k \times l} \qquad (74)$$

The derivative of a matrix w.r.t. a vector can be obtained as follows. Let:

$$\mathbf{A}\mathbf{b} = \begin{bmatrix} \mathbf{a}_1 & \cdots & \mathbf{a}_h \end{bmatrix} \begin{bmatrix} b_1 \\ \vdots \\ b_h \end{bmatrix} = \sum_{i=1}^{h} \mathbf{a}_i b_i \in \mathbb{R}^{k \times 1} \qquad (75)$$

Then:

$$\frac{\partial (\mathbf{A}\mathbf{b})}{\partial \mathbf{c}} = \sum_{i=1}^{h} \frac{\partial \mathbf{a}_i}{\partial \mathbf{c}} b_i + \sum_{i=1}^{h} \mathbf{a}_i \frac{\partial b_i}{\partial \mathbf{c}} \qquad (76)$$

Formally, (76) may also be written as:

$$\frac{\partial (\mathbf{A}\mathbf{b})}{\partial \mathbf{c}} = \frac{\partial \mathbf{A}}{\partial \mathbf{c}} \mathbf{b} + \mathbf{A} \frac{\partial \mathbf{b}}{\partial \mathbf{c}} \qquad (77)$$

Comparing (76) and (77) yields:

$$\frac{\partial \mathbf{A}}{\partial \mathbf{c}} \mathbf{b} = \sum_{i=1}^{h} \frac{\partial \mathbf{a}_i}{\partial \mathbf{c}} b_i \in \mathbb{R}^{k \times l} \tag{78}$$

$$\mathbf{A} \frac{\partial \mathbf{b}}{\partial \mathbf{c}} = \sum_{i=1}^{h} \mathbf{a}_i \frac{\partial b_i}{\partial \mathbf{c}} \in \mathbb{R}^{k \times l} \tag{79}$$

References

[1] E. Idà, T. Bruckmann, and M. Carricato, "Rest-to-rest trajectory planning for underactuated cable-driven parallel robots," *IEEE Transactions on Robotics*, vol. 35, no. 6, pp. 1338–1351, Dec 2019.

[2] J. Fink, N. Michael, S. Kim, and V. Kumar, "Planning and control for cooperative manipulation and transportation with aerial robots," *The International Journal of Robotics Research*, vol. 30, no. 3, pp. 324–334, 2011.

[3] L. Barbazza, D. Zanotto, G. Rosati, and S. K. Agrawal, "Design and optimal control of an underactuated cable-driven micro-macro robot," *IEEE Robotics and Automation Letters*, vol. 2, no. 2, pp. 896–903, April 2017.

[4] G. Previati, M. Gobbi, and G. Mastinu, "Measurement of the mass properties of rigid bodies by means of multi-filar pendulums – influence of test rig flexibility," *Mechanical Systems and Signal Processing*, vol. 121, pp. 31 – 43, 2019.

[5] L. Scalera, A. Gasparetto, and D. Zanotto, "Design and experimental validation of a 3-dof underactuated pendulum-like robot," *IEEE/ASME Transactions on Mechatronics*, vol. 25, no. 1, pp. 217–228, 2020.

[6] G. Abbasnejad and M. Carricato, "Direct geometrico-static problem of underconstrained cable-driven parallel robots with n cables," *IEEE Transactions on Robotics*, vol. 31, no. 2, pp. 468–478, April 2015.

[7] A. Berti, J.-P. Merlet, and M. Carricato, "Solving the direct geometrico-static problem of underconstrained cable-driven parallel robots by interval analysis," *The International Journal of Robotics Research*, vol. 35, no. 6, pp. 723–739, 2016.

[8] M. Carricato and J. Merlet, "Stability Analysis of Underconstrained Cable-Driven Parallel Robots," *IEEE Transactions on Robotics*, vol. 29, no. 1, pp. 288–296, Feb 2013.

[9] D. Surdilovic and J. Radojicic, "Practical stability of under-constrained cable-suspended parallel robots," in *Cable-Driven Parallel Robots*, A. Pott and T. Bruckmann, Eds. Cham: Springer International Publishing, 2019, pp. 85–98.

[10] D. Cunningham and H. H. Asada, "The winch-bot: A cable-suspended, under-actuated robot utilizing parametric self-excitation," in *2009 IEEE International Conference on Robotics and Automation*, May 2009, pp. 1844–1850.

[11] N. Zoso and C. Gosselin, "Point-to-point motion planning of a parallel 3-dof underactuated cable-suspended robot," in *2012 IEEE International Conference on Robotics and Automation*, May 2012, pp. 2325–2330.

[12] J. Park, O. Kwon, and J. H. Park, "Anti-sway trajectory generation of incompletely restrained wire-suspended system," *Journal of Mechanical Science and Technology*, vol. 27, no. 10, pp. 3171–3176, Oct 2013.

[13] S. Lefrançois and C. Gosselin, "Point-to-point motion control of a pendulum-like 3-dof underactuated cable-driven robot," in *2010 IEEE International Conference on Robotics and Automation*, 2010, pp. 5187–5193.

[14] S. W. Hwang, J.-H. Bak, J. Yoon, J. H. Park, and J.-O. Park, "Trajectory generation to suppress oscillations in under-constrained cable-driven parallel robots," *Journal of Mechanical Science and Technology*, vol. 30, no. 12, pp. 5689–5697, Dec 2016.

[15] S. W. Hwang, J.-H. Bak, J. Yoon, and J. H. Park, "Oscillation reduction and frequency analysis of under-constrained cable-driven parallel robot with three cables," *Robotica*, vol. 38, no. 3, pp. 375–395, 2020.

[16] E. Idà, S. Briot, and M. Carricato, "Robust trajectory planning of underactuated cable-driven parallel robot with 3 cables," in *Advances in Robot Kinematics 2020*, J. Lenarčič and B. Siciliano, Eds. Cham: Springer International Publishing, 2021, pp. 65–72.

[17] E. Idá, J.-P. Merlet, and M. Carricato, "Automatic self-calibration of suspended under-actuated cable-driven parallel robot using incremental measurements," in *Cable-Driven Parallel Robots*, A. Pott and T. Bruckmann, Eds. Cham: Springer International Publishing, 2019, pp. 333–344.

[18] R. de Rijk, M. Rushton, and A. Khajepour, "Out-of-plane vibration control of a planar cable-driven parallel robot," *IEEE/ASME Transactions on Mechatronics*, vol. 23, no. 4, pp. 1684–1692, 2018.

[19] M. Zarei, A. Aflakian, A. Kalhor, and M. T. Masouleh, "Oscillation damping of nonlinear control systems based on the phase trajectory length concept: An experimental case study on a cable-driven parallel robot," *Mechanism and Machine Theory*, vol. 126, pp. 377 – 396, 2018.

[20] M. R. Jafari Harandi, H. Damirchi, S. a. Khalilpour seyedi, and H. D. Taghirad, "Point-to-point motion control of an underactuated planar cable driven robot," in *2019 27th Iranian Conference on Electrical Engineering (ICEE)*, 2019, pp. 979–984.

[21] S. Briot, A. Pashkevich, and D. Chablat, "On the Optimal Design of Parallel Robots Taking Into Account Their Deformations and Natural Frequencies," in *ASME 2009 International Design Engineering Technical Conferences and Computers and Information in Engineering Conference*, 08 2009, pp. 367–376.

[22] W. Singhose, E. Crain, and W. Seering, "Convolved and simultaneous two-mode input shapers," *IEE Proceedings - Control Theory and Applications*, vol. 144, no. 6, pp. 515–520, Nov 1997.

[23] A. Pott, "Influence of pulley kinematics on cable-driven parallel robots," in *Latest Advances in Robot Kinematics*, J. Lenarcic and M. Husty, Eds. Dordrecht: Springer, 2012, pp. 197–204.

[24] D. Surdilovic, J. Radojicic, and J. Krüger, *Geometric Stiffness Analysis of Wire Robots: A Mechanical Approach*. Berlin, Heidelberg: Springer Berlin Heidelberg, 2013, pp. 389–404.

[25] M. Conconi and M. Carricato, "A new assessment of singularities of parallel kinematic chains," *IEEE Transactions on Robotics*, vol. 25, no. 4, pp. 757–770, Aug 2009.

[26] H. D. Taghirad, *Parallel robots: mechanics and control*. CRC press, 2013.

[27] G. H. Golub and C. F. Van Loan, *Matrix computations*. JHU press, 2013.

[28] Z. Cui, X. Tang, S. Hou, and H. Sun, "Research on controllable stiffness of redundant cable-driven parallel robots," *IEEE/ASME Transactions on Mechatronics*, vol. 23, no. 5, pp. 2390–2401, Oct 2018.

[29] S. Behzadipour and A. Khajepour, "Stiffness of Cable-based Parallel Manipulators With Application to Stability Analysis," *Journal of Mechanical Design*, vol. 128, no. 1, pp. 303–310, 04 2005.

[30] K. Kozak, I. Ebert-Uphoff, and W. Singhose, "Locally Linearized Dynamic Analysis of Parallel Manipulators and Application of Input Shaping to Reduce Vibrations ," *Journal of Mechanical Design*, vol. 126, no. 1, pp. 156–168, 03 2004.

[31] A. H. Nayfeh and D. T. Mook, *Nonlinear oscillations*. John Wiley & Sons, 2008.

[32] E. Idà, S. Briot, and M. Carricato, "Natural oscillations of underactuated cable-driven parallel robots - complete experiments data," 2020. [Online]. Available: http://dx.doi.org/10.21227/cdkb-fn05

[33] A. A. Kumar, J.-F. Antoine, P. Zattarin, and G. Abba, "Workspace analysis of a 4 cable-driven spatial parallel robot," in *ROMANSY 22 – Robot Design, Dynamics and Control*, V. Arakelian and P. Wenger, Eds. Cham: Springer International Publishing, 2019, pp. 204–212.

[34] M. F. Daqaq and Z. N. Masoud, "Nonlinear input-shaping controller for quay-side container cranes," *Nonlinear Dynamics*, vol. 45, no. 1, p. 149, Mar 2006.

EDOARDO IDÀ received the M.Sc. degree (with honors) in Mechanical Engineering in 2017 from the University of Bologna, and is currently a Ph.D. student in Mechanics and Advanced Engineering Sciences at the same university. His research interests focus on cable-driven robotic systems.
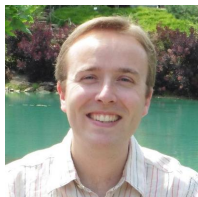
SÉBASTIEN BRIOT received the B.S. and M.S. degrees in mechanical engineering in 2004 and the Ph.D. degree in robotics (under the supervision of Prof. V. Arakelian) in 2007, from the Institut National des Sciences Appliquées de Rennes, Rennes, France. He was a Postdoctoral Fellow with the Ecole de Technologie Supérieure, Montreal, QC, Canada, in 2008. Since 2009, he has been a full-time CNRS Researcher with the Laboratoire des Sciences du Numérique de Nantes, Nantes, France, where he has been the Head of the ARMEN Research Team since 2017. He studies the impact of sensor-based controllers on the robot performance. He has authored 40 referred journal papers, two books, and three inventions. His research interests include the design optimization of robots and the analysis of their dynamic performance. Dr. Briot received the Best Ph.D. Thesis Award in Robotics from the French CNRS in 2007. In 2011, he received two other awards: the Award for the Best Young Researcher from the French Region Bretagne and the Award for the Best Young Researcher from the French Section of the American Society of Mechanical Engineering.

MARCO CARRICATO received the M.Sc. degree (with honors) in Mechanical Engineering in 1998 and the Ph.D. degree in mechanics of machines in 2002. He has been with the University of Bologna since 2004. He is currently a full professor. He was visiting researcher at the University of Florida (USA), at Laval University (Canada), at the University of Guanajuato (Mexico), at INRIA- Sophia Antipolis (France), at the Ecole Centrale of Nantes (France), and at the Hong Kong University of Science and Technology. He is an associate editor of the journal Mechanism and Machine Theory. He was awarded the AIMETA Junior Prize 2011 by the Italian Association of Theoretical and Applied Mechanics for outstanding results in the field of mechanics of machines. His research interests include robotic systems, servo-actuated automatic machinery and the theory of mechanisms.

• • •